

GAPSL: A Gradient-Aligned Parallel Split Learning on Heterogeneous Data

Zheng Lin, Ons Aouedi, *Member, IEEE*, Wei Ni, *Fellow, IEEE*, Symeon Chatzinotas, *Fellow, IEEE*, and Xianhao Chen, *Member, IEEE*

Abstract—The increasing complexity of neural networks poses significant challenges for democratizing FL on resource-constrained client devices. Parallel split learning (PSL) has emerged as a promising solution by offloading substantial computing workload to a server via model partitioning, shrinking client-side computing load, and eliminating the client-side model aggregation for reduced communication and deployment costs. Since PSL is *aggregation-free*, it suffers from severe training divergence stemming from gradient directional inconsistency across clients. To address this challenge, we propose GAPSL, a gradient-aligned PSL framework that comprises two key components: leader gradient identification (LGI) and gradient direction alignment (GDA). LGI dynamically selects a set of directionally consistent client gradients to construct a leader gradient that captures the global convergence trend. GDA employs a direction-aware regularization to align each client’s gradient with the leader gradient, thereby mitigating inter-device gradient directional inconsistency and enhancing model convergence. We evaluate GAPSL on a prototype computing testbed. Extensive experiments demonstrate that GAPSL consistently outperforms state-of-the-art benchmarks in training accuracy and latency.

Index Terms—Distributed machine learning, parallel split learning, gradient directional inconsistency, mobile edge computing.

I. INTRODUCTION

The Internet of Things (IoT) is experiencing rapid expansion, interconnecting billions of smart devices that continuously generate vast volumes of privacy-sensitive data [1], [2], [3], [4]. This unprecedented amount of data significantly advances the maturity of machine learning (ML) for enabling intelligent IoT applications. Conventional ML predominantly relies on centralized learning (CL), where raw data is collected and processed on a central server for model training [5], [6], [7], [8]. With the exponential growth of global data traffic—projected to reach 181 zettabytes by 2025 and 394 zettabytes by 2028 [9]—CL faces serious limitations in communication overhead and data privacy risks. Transmitting such large volumes of raw data incurs substantial communication overhead, and centralized storage and processing of sensitive data raise even more critical privacy concerns [10], [11]. To address these

Z. Lin and X. Chen are with the Department of Electrical and Electronic Engineering, University of Hong Kong, Pok Fu Lam, Hong Kong, China (e-mail: linzheng@eee.hku.hk; xchen@eee.hku.hk).

W. Ni is with Data61, CSIRO, Marsfield, NSW 2122, Australia, and the School of Computing Science and Engineering, and the University of New South Wales, Kensington, NSW 2052, Australia (e-mail: wei.ni@ieee.org).

O. Aouedi and S. Chatzinotas are with the Interdisciplinary Centre for Security, Reliability and Trust (SnT), University of Luxembourg, L-1855 Luxembourg, Luxembourg (e-mail: ons.aouedi@uni.lu; symeon.chatzinotas@uni.lu).

(Corresponding author: Xianhao Chen)

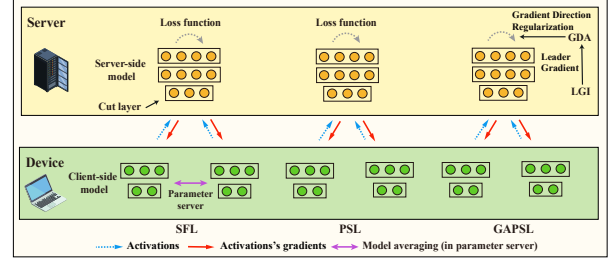


Fig. 1: The comparison of SFL, PSL, and GAPSL frameworks, where SFL relies on a parameter server to aggregate client-side models and PSL streamlines the training process by eliminating the client-side model aggregation.

issues, federated learning (FL) [12], [13] has emerged as an alternative that enables collaborative model training across client devices by exchanging model parameters rather than raw data [14], [15], [16]. While FL alleviates privacy and bandwidth concerns, it encounters scalability bottlenecks as ML models scale up [17], [18]. For instance, training and deploying large-sized models, such as Gemini Nano-2 with 3.25 billion parameters (3GB for 32-bit floats), can exceed the computing and storage capabilities of resource-constrained client devices [19], [20].

Split federated learning (SFL) [21] offers a promising solution to addressing the weaknesses of FL by offloading the computation-intensive workload from client devices to a server via model partitioning. By integrating the model partitioning of split learning (SL) with parallel training of FL, SFL enables multiple edge devices to collaboratively train a shared model. Despite its advantages, SFL still faces a severe limitation. It relies on a third-party parameter server¹ to aggregate client-side models, incurring considerable communication and deployment costs. To address this issue, parallel split learning (PSL) [26], [27] has been proposed as an efficient variant of SFL. PSL streamlines the training procedure of SFL by eliminating the need for client-side model aggregation, substantially reducing communication overhead and simplifying system deployment. A comparative illustration of SFL and PSL is presented in Fig. 1.

While PSL offers a lightweight and communication-efficient alternative to SFL by eliminating client-side model aggregation,

¹The parameter server cannot exchange information with the main server. Otherwise, this collusion can lead to severe privacy risks because the server knows both activations and model parameters from clients [22], [23], [24], [25].

it is inherently more vulnerable to data heterogeneity. In contrast to FL and SFL, where periodic model aggregation serves as a statistical calibration mechanism to mitigate the impact of non-independent and identically distributed (non-IID) data, PSL operates without any such aggregation [28]. As a result, each client device independently generates activations based solely on its local data, which are often severely skewed due to class imbalance or covariate shift [29], [30]. These semantically inconsistent and statistically biased activations lead to divergent gradient directions during the back-propagation (BP) process on the server. The resulting gradient updates exhibit a dual nature: while some gradients align with the global convergence direction, others, dominated by local inductive biases, introduce noise or even adversarial updates. PSL exhibits much higher gradient divergence than SFL due to the lack of client-side model aggregation. Such conflicting gradients without calibration not only fail to correct activation biases but also exacerbate gradient directional inconsistency, ultimately causing poor learning performance or even convergence failure [31]. We have conducted empirical studies in Section II and identified gradient directional inconsistency as an underlying cause of the convergence failure of PSL. This analysis provides key insights and motivation for the design of GAPSL, which explicitly addresses gradient inconsistency to enhance training stability and convergence efficiency.

To tackle the above challenge, as shown in Fig. 1, we propose a gradient-aligned PSL framework, named GAPSL, with a gradient-aligned mechanism to mitigate the training divergence caused by conflicting gradients across client devices. GAPSL comprises two key components. First, to identify a gradient direction reflecting the global convergence trend, we design a leader gradient identification (LGI) mechanism that dynamically selects a set of directionally consistent client gradients to construct a leader gradient. Second, to enhance inter-device gradient alignment and mitigate directional conflicts during training, we develop a gradient direction alignment (GDA) scheme that employs the direction-aware regularization to steer each device’s gradient toward the leader gradient. The key contributions of this paper are summarized as follows:

- To the best of our knowledge, GAPSL is the first PSL framework that resolves the problem of gradient directional inconsistency, enabling efficient and stable SL without client-side model aggregation.
- We design LGI to dynamically select a set of gradients based on directional consistency and construct a leader gradient reflecting the global convergence direction.
- We devise GDA to adaptively align each client’s gradient with the leader gradient via direction-aware regularization, thereby mitigating gradient directional conflicts and improving model convergence.
- We evaluate GAPSL on a prototype computing testbed with extensive experiments. The results demonstrate that GAPSL outperforms state-of-the-art frameworks.

The rest of this paper is organized as follows. Section II motivates the design of GAPSL and Section III elaborates on the system design. Section IV introduces the system implementation, followed by performance evaluation in Section V. Related works and technical limitations are discussed in

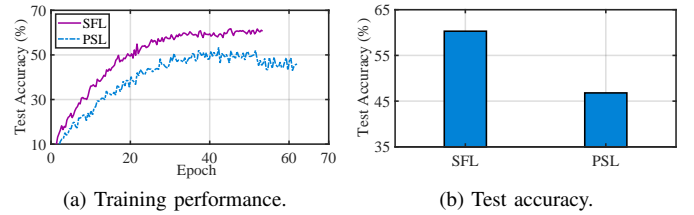


Fig. 2: The training performance (a) and test accuracy (b) of SFL and PSL on CIFAR-10 using VGG-16.

Section VI. Finally, conclusions are presented in Section VII.

II. CHALLENGE AND MOTIVATION

To elucidate the fundamental limitations of PSL and motivate the design of GAPSL, we conduct empirical studies to investigate the impacts of i) the lack of client-side model aggregation and ii) gradient directional inconsistency on training performance.

A. Lack of Client-side Model Aggregation

While PSL reduces communication and deployment costs by eliminating client-side model aggregation, it inherently lacks model synchronization [26], [27]. Thus, each client device generates semantically inconsistent and statistically biased activations based solely on its non-IID local dataset, which are directly used to train the model. Without aggregation to calibrate these biases, the semantic discrepancies accumulate as training progresses, destabilizing the learning process and impeding convergence.

To gain a deeper understanding of the impact of lacking client-side model aggregation in PSL, we compare its performance with SFL using the VGG-16 neural network [32] on the CIFAR-10 dataset [33]. Unless otherwise specified, this configuration remains consistent throughout the whole Section II. Following prior studies [34], [35], [36], we adopt Dirichlet data partitioning to set the degree of data heterogeneity controlled by parameter α , where a smaller α represents a higher degree of data heterogeneity, indicating that each client device holds data from a more skewed or narrower subset of classes. In our experiment, we set the Dirichlet partitioning parameter α to 0.1. Fig. 2a illustrates that PSL exhibits significantly slower and less stable convergence compared to SFL. PSL fails to achieve model convergence entirely, indicating a substantial collapse in learning stability under high data heterogeneity. Furthermore, Fig. 2b reveals that PSL consistently achieves lower test accuracy than SFL. These observations suggest that PSL suffers not only from significantly degraded performance but also from impaired convergence stability in the non-IID setting. In contrast, SFL demonstrates greater robustness, primarily due to its periodic client-side model aggregation, which helps mitigate semantic drift across client devices. Motivated by this, it is imperative to develop coordination mechanisms for PSL that enforce semantic consistency across clients, thereby improving both convergence robustness and model performance.

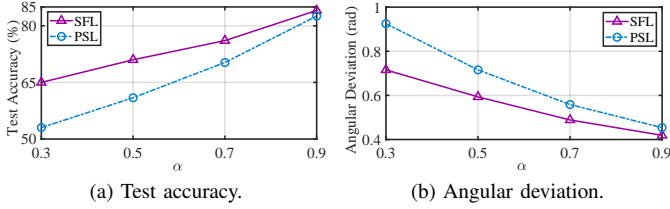


Fig. 3: The test accuracy (a) and average angular deviation (b) versus degree of data heterogeneity on CIFAR-10 using VGG-16.

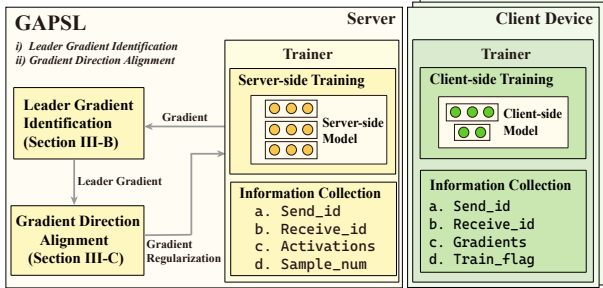


Fig. 4: An overview of GAPSL architecture.

B. Gradient Directional Inconsistency

While Section II-A underscores that the lack of client-side model aggregation deteriorates the training performance of PSL, the underlying cause stems from inconsistent gradient directions across client devices. In PSL, each device independently performs forward propagation (FP) and BP on its local dataset, without any inter-device aggregation or coordination. In the non-IID setting, this independence drives each device to optimize toward a client-specific objective, resulting in gradients that diverge from the global optimization direction. While some client gradients may align with the global direction, others, biased by skewed data distribution, can contribute high-variance or even conflicting updates, thereby hindering model convergence.

To validate the above intuition, we compare the test accuracy and gradient directional consistency of SFL and PSL under varying degrees of data heterogeneity. Fig. 3a illustrates that the test accuracy of PSL is consistently lower than that of SFL, with the performance gap widening notably as data heterogeneity increases (i.e., smaller α). This performance degradation aligns closely with the gradient behavior shown in Fig. 3b, where we measure gradient directional consistency using the average angular deviation between gradients² (i.e., a smaller angular deviation indicates more consistent gradient directions). The results show that PSL exhibits significantly higher angular deviation than SFL, particularly under high data heterogeneity, indicating more severe gradient misalignment due to the lack of client-side coordination. Taken together, these results reveal a strong correlation between degraded performance and gradient directional inconsistency in PSL. As client gradients become

²Let \mathbf{g}_i and \mathbf{g}_j denote the gradients computed by the i -th and j -th client devices on their local datasets. The pairwise angular deviation is defined as $\arccos\left(\frac{\langle \mathbf{g}_i, \mathbf{g}_j \rangle}{\|\mathbf{g}_i\| \cdot \|\mathbf{g}_j\|}\right)$. The values reported in Fig. 3b plot the average of these deviations across all distinct device pairs, quantifying the overall directional inconsistency.

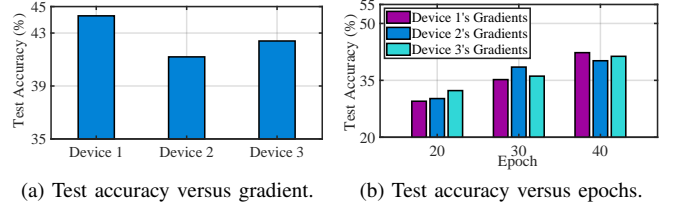


Fig. 5: The PSL performance of training a model with the gradient from a single client device only (discarding others' gradients) on CIFAR-10 using VGG-16 under the non-IID setting.

increasingly misaligned, the global model struggles to converge effectively. This provides compelling empirical evidence that gradient directional inconsistency is a key bottleneck for PSL under the non-IID setting.

III. SYSTEM DESIGN

A. Overview

In this section, we propose GAPSL, a gradient-aligned PSL framework designed to enable efficient and stable model training without client-side model aggregation. As illustrated in Fig. 4, GAPSL consists of two key components: i) *leader gradient identification* (LGI) (Section III-B), which identifies the global convergence direction by selectively aggregating directionally consistent client gradients; and ii) *gradient direction alignment* (GDA) (Section III-C), which enforces inter-device gradient consistency via direction-aware regularization.

In GAPSL, the global model is partitioned into two sub-models: a client-side model deployed on client devices and a server-side model hosted on the server. The training workflow for one training round consists of the following three steps: i) each client device executes FP on the client-side model with its local dataset and transmits the resulting activations to the server; ii) the server employs LGI to construct a leader gradient and then utilizes GDA to regulate each device's gradient direction, followed by BP on the server-side model to generate activation's gradients; and iii) the server sends all generated gradients to the client device for updating their respective client-side models via BP. Notably, since LGI and GDA are executed entirely on the server, GAPSL incurs the same communication overhead as standard PSL (i.e., exchanging activations/gradients), which is strictly lower than SFL due to the elimination of client-side model parameter transmissions.

B. Leader Gradient Identification

As discussed in Section II, the lack of client-side model aggregation in PSL exacerbates the divergence of gradient directions across client devices. Consequently, the contribution of individual devices to the global model convergence is highly uneven: while some gradients promote model convergence, others may introduce noise or adversarial updates driven by local data biases. To empirically validate this effect, we conduct an experiment where the model is trained using the gradients from a single client device only³. Fig. 5a demonstrates

³In reality, PSL cannot do this because a client cannot access another client's gradients to update its model.

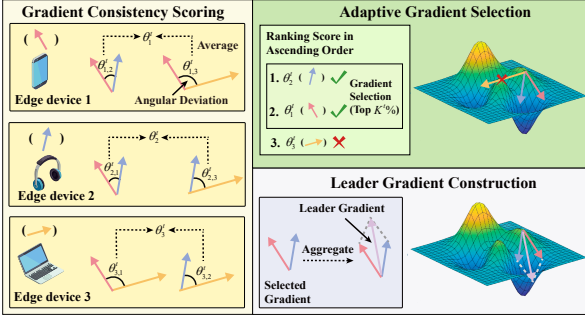


Fig. 6: An illustration of LGI.

significant variance in test accuracy across client devices, and Fig. 5b reveals that the most contributive gradient changes across training epochs.

These observations point to a key insight: *due to gradient direction discrepancies, treating all client updates equally can lead to sub-optimal updates and hinder convergence.* This underscores the need to identify the underlying global convergence trend to guide the training process. Although PSL forgoes model aggregation and thus does not access client-side gradients, the server naturally computes gradients for its own model segment for each client. Since the server takes activations from client-side models as input, these server-side gradients inherently capture training divergence stemming from client-side data and model heterogeneity. Motivated by this, we propose the LGI mechanism, as shown in Fig. 6. LGI dynamically selects a subset of directionally consistent server-side gradients (i.e., those closely aligned with the global convergence direction) to construct a leader gradient. This leader gradient serves as a directional reference (or anchor) for the subsequent gradient alignment in Section III-C. The LGI mechanism consists of the following three key components:

1) *Gradient Consistency Scoring*: Existing approaches for assessing the gradient contribution in distributed ML typically rely on gradient magnitudes [37], [38], [39], assuming that larger gradients convey more informative updates. However, this assumption often falters in non-IID settings, as large gradients may deviate from the global convergence direction and thus impede model convergence. In contrast, small but directionally consistent gradients are more effective in promoting stable convergence. To rectify this, we propose a gradient consistency score that quantifies the directional alignment of a device’s gradient relative to others. For the t -th training round, the gradient consistency score of the i -th client device θ_i^t is defined as the average angular deviation between its gradient and those of other participating devices:

$$\theta_i^t = \frac{1}{|\mathcal{S}| - 1} \sum_{\substack{j \in \mathcal{S} \\ j \neq i}} \theta_{i,j}^t, \text{ where } \theta_{i,j}^t = \arccos \left(\frac{\langle \mathbf{g}_i^t, \mathbf{g}_j^t \rangle}{\|\mathbf{g}_i^t\| \cdot \|\mathbf{g}_j^t\|} \right), \quad (1)$$

where $\mathcal{S} = \{1, 2, \dots, S\}$ denotes the set of participating client devices, $\theta_{i,j}^t$ represents the angular deviation between the gradients of i -th and j -th client device, \mathbf{g}_k^t is the gradient of the k -th client device for the server-side model, $\arccos(\cdot)$,

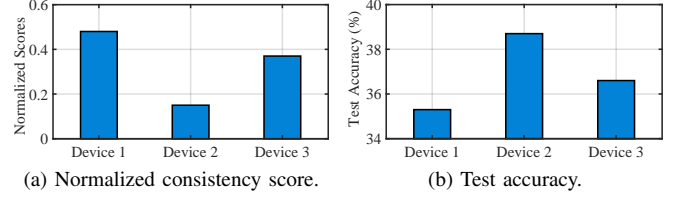


Fig. 7: The normalized gradient consistency scores and corresponding test accuracies of client devices over 30 epochs on CIFAR-10 using VGG-16.

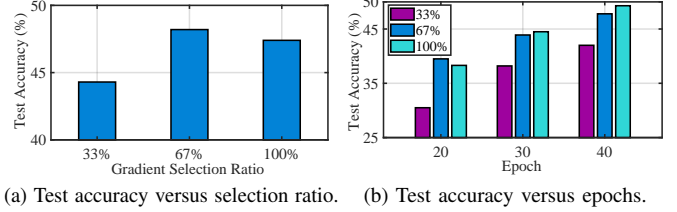


Fig. 8: The test accuracy versus gradient selection ratio and epochs on CIFAR-10 using VGG-16.

$\langle \cdot, \cdot \rangle$, and $\|\cdot\|$ denote the inverse cosine function, the inner product operation, and the Euclidean norm, respectively.

Eqn. (1) yields two key insights regarding the geometric properties of client updates: i) A smaller θ_i^t indicates that the client’s gradient is directionally consistent with the majority, implying a higher likelihood of constructive contribution to the global optimization; and ii) A larger θ_i^t indicates severe directional inconsistency, suggesting that the client’s gradient may introduce noise or conflicting updates. As illustrated in Fig. 7, the client device with a lower gradient consistency score consistently yields superior test accuracy. This result reveals the effectiveness of the proposed consistency scoring in identifying directionally consistent gradients.

2) *Adaptive Gradient Selection*: To mitigate the adverse effects of conflicting updates, we propose an adaptive gradient selection strategy that prioritizes gradients with stronger directional consistency (i.e., those with lower gradient consistency scores as defined in Eqn. (1)). These selected gradients form the basis for constructing the leader gradient, which serves as a directional anchor for guiding the model training (See Section III-B3). While gradient consistency scoring helps quantify the quality of individual gradients, a key design question arises: *how many gradients should be selected?*

We introduce an adaptive gradient selection ratio $K\%$, defined as the time-varying proportion of top-ranked gradients (i.e., sort gradients in ascending order of consistency scores) selected. This ratio governs a fundamental trade-off between gradient directional alignment and information diversity: selecting too few gradients enhances gradient consistency but limits representational diversity, while selecting too many increases the risk of incorporating divergent or noisy gradients. This theoretical trade-off is empirically corroborated by Fig. 8a, which demonstrates that extremes in selection ratios degrade model performance. Furthermore, Fig. 8b reveals that the optimal selection ratio is not static but varies across training

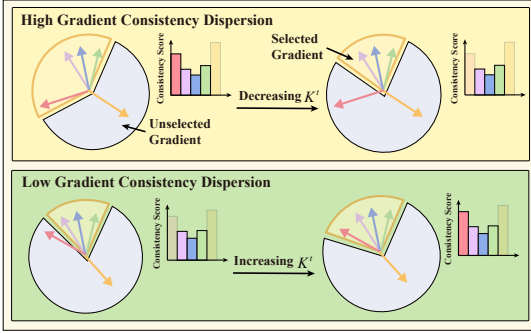
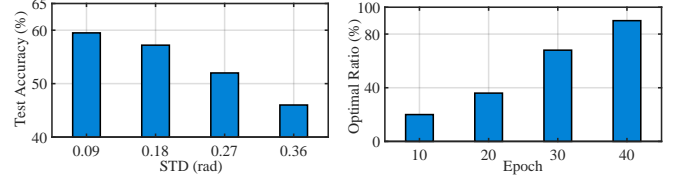


Fig. 9: The impact of gradient consistency dispersion on gradient selection.

epochs. These observations underscore the inadequacy of fixed selection ratios and highlight the necessity of an adaptive mechanism capable of adjusting the selection ratio for training dynamics.

To design an adaptive gradient selection mechanism, we begin with two intuitions: i) *Gradient consistency dispersion*: The dispersion of gradient consistency scores serves as an indicator of directional consensus among client gradients. As shown in Fig. 9, a high dispersion implies substantial disagreement in gradient directions; a stringent selection strategy is imperative to filter out conflicting updates and stabilize training. Conversely, low dispersion suggests a tight clustering of gradient directions, allowing for the inclusion of mid-ranked gradients to enhance information utilization without compromising training performance; ii) *Training dynamics*: The optimal gradient selection ratio is not static but evolves throughout the training process. Crucially, rather than requiring exhaustive task-specific manual tuning that would introduce severe hyperparameter optimization overhead, the gradient selection ratio is designed to dynamically self-adjust. During the early stages, a conservative selection ratio is essential to enforce strict directional alignment and suppress noisy gradients. As the model converges, progressively expanding the selection to include a broader range of gradients introduces beneficial diversity and thus improves model generalization. To validate these two design principles, we conduct two empirical studies using the standard deviation (STD) of gradient consistency scores to quantify gradient directional dispersion⁴. Fig. 10a illustrates that test accuracy exhibits a consistent decline as the STD increases, indicating that higher dispersion undermines training performance. Furthermore, an exhaustive search for the optimal selection ratio across training epochs, as shown in Fig. 10b, reveals a monotonic increase in the optimal selection ratio. This trend confirms the necessity of a time-varying selection that transitions from strict alignment to broader participation as the global model converges.

⁴The gradient consistency score captures the angular deviation of each client’s gradient relative to the others, reflecting how well it aligns with the collective update direction. The STD of these scores indicates the degree of directional agreement: a small STD indicates that most client gradients deviate by similar angles, suggesting strong gradient directional alignment among clients; in contrast, a large STD implies significant variation, with some gradients closely aligned and others highly deviated.



(a) Test accuracy versus selection ratio. (b) Test accuracy versus epochs.

Fig. 10: The test accuracy versus STD of gradient consistency score and optimal selection ratio versus epochs on CIFAR-10 using VGG-16.

The design of our adaptive selection ratio is built on the empirical insights observed in Fig. 10. The negative correlation between gradient dispersion and training performance (Fig. 10a) mandates a stability-aware penalty mechanism. We encode this by normalizing the current dispersion $\nu(\theta^t)$ against its historical maximum to derive a relative stability score, which adaptively constricts the selection ratio as directional divergence intensifies. Temporally, the linear growth of the optimal selection ratio (Fig. 10b) motivates the incorporation of a linear time-scaling term, $\frac{t}{T}$, designed to progressively relax selection constraints as the model converges. We employ a multiplicative coupling of these two factors that functions as a robust gating mechanism: it ensures that the selection ratio approaches its upper bound K_{max} if and only if the training is sufficiently advanced and the gradients remain directionally consistent. This design explicitly prevents the inclusion of conflicting updates for high directional divergence. Therefore, the selection ratio at the t -th training round is defined as:

$$K^t = K_{min} + \left(\frac{t}{T} \frac{\nu_{max}^t - \nu(\theta^t)}{\nu_{max}^t - \nu_{min}^t} \right) (K_{max} - K_{min}), \quad (2)$$

where $\theta^t = \{\theta_i^t\}_{i=1}^S$ is the set of gradient consistency scores for all client devices in the t -th training round; $\nu(\theta)$ represents the STD of directional consistency scores, quantifying the dispersion of gradient directions; K_{min} and K_{max} are lower and upper bounds of the feasible selection ratio range⁵, respectively; $\frac{\nu_{max}^t - \nu(\theta^t)}{\nu_{max}^t - \nu_{min}^t}$ functions as the relative stability score, which maps the current gradient volatility into a normalized range $[0, 1]$, where ν_{min}^t and ν_{max}^t are dynamically updated via tracking the minimum and maximum observed values of $\nu(\theta^t)$ observed up to the t -th round.

Remark. In Eqn. (2), the term $\nu(\theta^t)$ serves as a key indicator for adaptive adjustment of the selection ratio K^t : when dispersion is high (i.e., gradients are misaligned), K^t is reduced to exclude potentially conflicting updates; when dispersion is low (i.e., gradients are well-aligned), a larger K^t is enabled to incorporate more client contributions. In addition, the temporal scaling term $\frac{t}{T}$ (T denotes the pre-scheduled total number of training rounds, requiring no additional task-specific tuning) introduces a progressive increase in K^t over the model training. This design encourages more conservative updates during the early stages to prioritize gradient stability and allows

⁵ K_{min} and K_{max} can be pre-set based on data heterogeneity, e.g., smaller values are preferred for highly non-IID datasets to reduce conflicting updates, while larger values suit more homogeneous datasets to speed up convergence.

Algorithm 1: Leader Gradient Identification

Input: $\mathcal{S}, K_{\min}, K_{\max}, \nu_{\min}^t, \nu_{\max}^t, t,$ and T
Output: $\mathbf{g}_{\text{lead}}^t$

```

1 Gradient Consistency Scoring:
2   foreach  $i \in \mathcal{S}$  do
3      $\theta_i^t = \frac{1}{|\mathcal{S}|-1} \sum_{j \in \mathcal{S}, j \neq i} \arccos\left(\frac{\langle \mathbf{g}_i, \mathbf{g}_j \rangle}{\|\mathbf{g}_i\| \cdot \|\mathbf{g}_j\|}\right)$  //
       Compute Angular Deviation;
4   end
5    $\boldsymbol{\theta}^t \leftarrow \{\theta_i^t\}_{i=1}^S$ ;
6 Adaptive Gradient Selection:
7    $\nu(\boldsymbol{\theta}^t) \leftarrow \text{Std}(\boldsymbol{\theta}^t)$  // Compute Standard Deviation;
8    $\nu_{\min}^t \leftarrow \min(\nu_{\min}^{t-1}, \nu(\boldsymbol{\theta}^t))$ ;
9    $\nu_{\max}^t \leftarrow \max(\nu_{\max}^{t-1}, \nu(\boldsymbol{\theta}^t))$ ;
10   $K^t = K_{\min} + \left(\frac{\nu_{\max}^t - \nu(\boldsymbol{\theta}^t)}{\nu_{\max}^t - \nu_{\min}^t}\right) (K_{\max} - K_{\min})$  //
       Calculate Gradient Selection Ratio;
11 Leader Gradient Construction:
12  Sort  $\mathcal{S}$  by  $D_i^t$  in ascending order;
13   $\tilde{\mathcal{S}}^t = \{i \in \mathcal{S} \mid \pi(\theta_i^t) \leq \lceil K^t\% \cdot |\mathcal{S}| \rceil\}$  // Select
       Top- $K^t\%$  client devices;
14   $\tilde{\mathcal{G}}^t \leftarrow \{\mathbf{g}_i^t \mid i \in \tilde{\mathcal{S}}^t\}$ ;
15   $\mathbf{g}_{\text{lead}}^t \leftarrow \frac{1}{|\tilde{\mathcal{G}}^t|} \sum_{\mathbf{g}_i^t \in \tilde{\mathcal{G}}^t} \mathbf{g}_i^t$  // Construct Leader
       Gradient;
16 return  $\mathbf{g}_{\text{lead}}^t$ 

```

for broader client gradient participation in later stages, which improves model generalization as training converges.

3) *Leader Gradient Construction:* With the adaptive selection ratio K^t established, the final step of the LGI is to construct a leader gradient, a robust estimate of the global optimization direction that serves as a directional anchor for gradient alignment in Section III-C. We first rank all client gradients in ascending order of their consistency scores, such that lower scores (indicating greater alignment) are ranked higher. Then, we select the top $\lceil K^t\% \cdot |\mathcal{S}| \rceil$ client devices to form the gradient subset, as given by

$$\tilde{\mathcal{S}}^t = \{i \in \mathcal{S} \mid \pi(\theta_i^t) \leq \lceil K^t\% \cdot |\mathcal{S}| \rceil\}, \quad (3)$$

where $\pi(\theta_i^t)$ denotes the ascending rank index of device i 's consistency score (i.e., lower scores imply higher consistency). The leader gradient is then computed via the selective aggregation of the gradient subset $\tilde{\mathcal{G}}^t = \{\mathbf{g}_i^t \mid i \in \tilde{\mathcal{S}}^t\}$:

$$\mathbf{g}_{\text{lead}}^t = \frac{1}{|\tilde{\mathcal{G}}^t|} \sum_{\mathbf{g}_i^t \in \tilde{\mathcal{G}}^t} \mathbf{g}_i^t. \quad (4)$$

By exclusively incorporating directionally consistent updates, this construction effectively filters out statistical outliers and adversarial noise. As a result, the leader gradient provides a noise-resilient and directionally reliable proxy for the true global descent direction. The complete LGI procedure is summarized in **Algorithm 1**.

C. Gradient Direction Alignment

Following the construction of the leader gradient via LGI (Section III-B), we obtain a directional anchor that captures

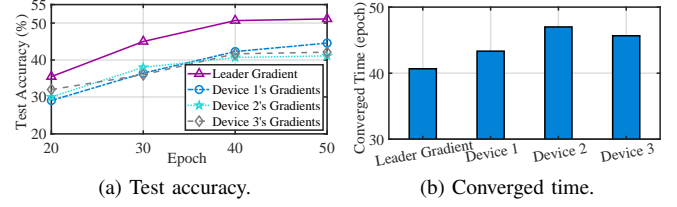


Fig. 11: The test accuracy and converged time via leader gradient and individual gradients on CIFAR-10 using VGG-16.

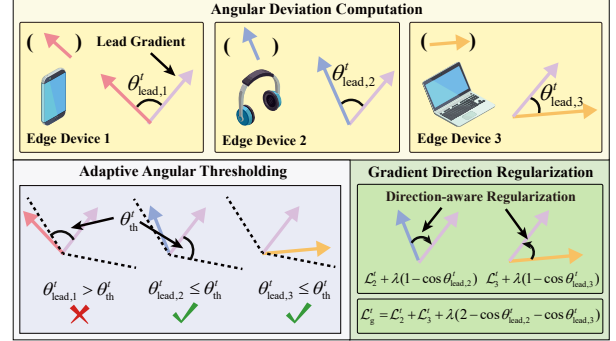


Fig. 12: An illustration of GDA.

the global optimization trend. Empirical validation in Fig. 11 demonstrates that models updated with this leader gradient significantly outperform those relying on individual gradients in test accuracy and convergence speed. These results underscore the potential of the leader gradient to guide or correct client gradient directions for enhancing training performance.

In light of this, we propose the GDA mechanism, as illustrated in Fig 12, to rectify the optimization drift induced by data heterogeneity. Rather than naively forcing all local updates to align with the leader gradient—which risks model degradation due to extreme statistical outliers—GDA adopts a robust two-stage alignment strategy. First, it employs an adaptive angular threshold to identify and exclude severely divergent gradient updates. Subsequently, it applies direction-aware regularization exclusively to the remaining viable clients. This selective alignment ensures that the global model assimilates beneficial local representations while strictly isolating destructive noise. Specifically, the GDA framework comprises the following three key components:

1) *Angular Deviation Computation:* To quantify the alignment between a device's local update and the global optimization direction, GDA computes the angular deviation between each device's gradient and the leader gradient \mathbf{g}_{lead} (derived via LGI in Section III-B). For the t -th training round, the angular deviation between the device i ' gradient and the leader gradient is calculated as

$$\theta_{\text{lead},i}^t = \arccos\left(\frac{\langle \mathbf{g}_i^t, \mathbf{g}_{\text{lead}}^t \rangle}{\|\mathbf{g}_i^t\| \cdot \|\mathbf{g}_{\text{lead}}^t\|}\right). \quad (5)$$

Remark. This angular metric serves as a geometric indicator of gradient alignment: A small $\theta_{\text{lead},i}$ (approaching 0) indicates that the device's gradient is well-aligned and directionally consistent with the global convergence direction. Conversely, a large $\theta_{\text{lead},i}$ (beyond $\frac{\pi}{2}$) suggests a conflicting update direction,

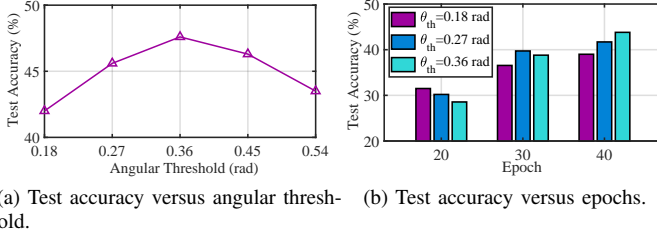


Fig. 13: The test accuracy versus angular threshold and epochs on CIFAR-10 using VGG-16.

stemming from severe data heterogeneity or noise. This angular metric provides a principled geometric basis for the subsequent coordination mechanisms, including adaptive thresholding and gradient direction regularization.

2) *Adaptive Angular Thresholding*: As discussed in Section II-B, client gradients of PSL often exhibit significant directional divergence under non-IID data. Directly aggregating all client gradients, regardless of their alignment with the global optimization direction, may introduce conflicting updates that exacerbate optimization drift and impede model convergence. Consequently, filtering gradients with excessive angular deviations is a prerequisite for effective alignment. While employing a fixed angular threshold θ_{th} offers a straightforward solution, allowing only client gradients whose angular deviation satisfies $\theta_{lead,i}^t \leq \theta_{th}$ to participate in the alignment process, it is inherently rigid and fails to accommodate the evolving gradient dynamics. Fig. 13 reveals the limitations of fixed thresholding. Fig. 13a indicates that extreme thresholds yield sub-optimal performance: overly stringent thresholds discard informative gradients, while overly loose ones admit conflicting noise. Furthermore, Fig. 13b reveals that the optimal threshold changes as training progresses, underscoring the necessity of a dynamic angular threshold.

To this end, we propose an adaptive angular thresholding mechanism. Since gradient consistency is relative to the distribution of the client gradients for the current training round, using fixed or historical standards is ineffective for distinguishing valid updates from noise. For instance, a larger angular deviation might be acceptable in a high-variance scenario but considered an outlier when gradients are well-aligned. Therefore, effective filtering requires a distribution-based approach that adapts to the current distribution. We avoid using historical min-max scaling because it is sensitive to outliers, i.e., a single gradient with an extreme angle can significantly skew the normalization range, rendering the filter ineffective. Instead, we formulate the threshold by leveraging the first and second-order statistics of the current gradient distribution to construct a robust confidence boundary. In the t -th training round, the angular threshold is derived as:

$$\theta_{th}^t = \max \left(\min \left(\mu(\boldsymbol{\theta}_{lead}^t) - \eta \nu(\boldsymbol{\theta}_{lead}^t), \frac{\pi}{2} \right), 0 \right), \quad (6)$$

where $\boldsymbol{\theta}_{lead}^t = \{\theta_{lead,i}^t\}_{i=1}^S$ is the set of gradient angular deviation for all devices in the t -th round, $\mu(\cdot)$ and $\nu(\cdot)$ denote the mean and standard deviation operations, respectively, and η controls the sensitivity of the threshold to gradient direction dispersion. Specifically, a larger η imposes a more conservative

Algorithm 2: Gradient Direction Alignment

Input : $\mathcal{S}, \mathbf{g}_{lead}^t, \lambda$
Output : \mathcal{L}_g^t

- 1 Angular Deviation Computation:
 - 2 **foreach** $i \in \mathcal{S}$ **do**
 - 3 $\theta_{lead,i}^t = \arccos \left(\frac{\langle \mathbf{g}_i^t, \mathbf{g}_{lead}^t \rangle}{\|\mathbf{g}_i^t\| \cdot \|\mathbf{g}_{lead}^t\|} \right)$ // Angular Deviation;
 - 4 **end**
 - 5 $\boldsymbol{\theta}_{lead}^t = \{\theta_{lead,i}^t\}_{i=1}^S$;
- 6 Adaptive Thresholding:
 - 7 $\mu(\boldsymbol{\theta}_{lead}^t) \leftarrow \text{Mean}(\boldsymbol{\theta}_{lead}^t)$;
 - 8 $\nu(\boldsymbol{\theta}_{lead}^t) \leftarrow \text{Std}(\boldsymbol{\theta}_{lead}^t)$;
 - 9 $\theta_{th}^t = \max \left(\min \left(\mu(\boldsymbol{\theta}_{lead}^t) - \eta \nu(\boldsymbol{\theta}_{lead}^t), \frac{\pi}{2} \right), 0 \right)$ // Adaptive Threshold;
 - 10 $\hat{\mathcal{S}}^t = \{i \in \mathcal{S} \mid \theta_{lead,i}^t \leq \theta_{th}^t\}$;
- 11 Gradient Direction Regularization:
 - 12 **foreach** $i \in \hat{\mathcal{S}}^t$ **do**
 - 13 $\tilde{\mathcal{L}}_i^t = \mathcal{L}_i^t + \lambda(1 - \cos \theta_{lead,i}^t)$ // Regularized Local Loss;
 - 14 **end**
 - 15 $\mathcal{L}_g^t = \sum_{i \in \hat{\mathcal{S}}^t} \tilde{\mathcal{L}}_i^t$;
 - 16 **return** \mathcal{L}_g^t

threshold, aggressively penalizing and discarding gradients under high directional variance. The threshold is capped at $\frac{\pi}{2}$ to exclude gradients with opposite directions, which could destabilize model training. Consequently, only clients satisfying $\theta_{lead,i}^t \leq \theta_{th}^t$ are selected for the subsequent gradient direction alignment (Section III-C3).

Remark. The adaptive angular threshold in Eqn. (6) provides a dynamic adaptation based on the statistical characteristics of client gradients. The mean $\mu(\boldsymbol{\theta}_{lead}^t)$ serves as the central reference, while the standard deviation $\nu(\boldsymbol{\theta}_{lead}^t)$ acts as a penalty for gradient directional inconsistency. Specifically, when gradient directions are well-aligned (i.e., low dispersion), the threshold is relaxed to allow broader client participation to accelerate convergence. Conversely, when gradient dispersion is high, the threshold is automatically tightened to enforce a stricter filter against noise.

3) *Gradient Direction Regularization*: Building upon the filtering of the adaptive thresholding, we introduce a direction-aware regularization term into the local loss function to rectify the updates of selected clients.

We augment the local loss with a nonlinear geometric regularization term $(1 - \cos \theta_{lead,i}^t)$. The adoption of this cosine-based form is motivated by two key properties. First, it maps angular deviation to a smooth, differentiable metric value within $[0, 1]$, ensuring numerical stability during BP. Second, the regularization term exhibits a vanishing characteristic near alignment: as $\theta_{lead,i}^t \rightarrow 0$, it naturally decays to zero. This guarantees that once the client gradient is well-aligned, the regularization term vanishes, allowing the model updates to be driven solely by the local loss function. For the i -th selected client device at the t -th training round (i.e., $i \in \hat{\mathcal{S}}^t$, where

$\widehat{\mathcal{S}}^t = \{i \in \mathcal{S} \mid \theta_{\text{lead},i}^t \leq \theta_{\text{th}}^t\}$, the regularized local loss⁶ is given by

$$\widetilde{\mathcal{L}}_i^t = \mathcal{L}_i^t + \lambda(1 - \cos \theta_{\text{lead},i}^t), \quad (7)$$

where \mathcal{L}_i denotes the original local loss, $\theta_{\text{lead},i}^t$ is the angular deviation between the i -th client device's gradient and the leader gradient, and $\lambda > 0$ represents a regularization coefficient.

Remark. The design of angular regularization in (7) is both adaptive and robust. Since the selected $\theta_{\text{lead},i}^t$ is restricted to $[0, \frac{\pi}{2}]$ via the adaptive thresholding in (6), the regularization function exhibits a strict monotonic increase across this domain. As $\theta_{\text{lead},i}^t \rightarrow 0$, indicating strong directional alignment, the penalty diminishes to zero and thereby preserves the original update. In contrast, as $\theta_{\text{lead},i}^t \rightarrow \frac{\pi}{2}$, the penalty reaches its maximum, effectively suppressing updates that are nearly orthogonal to the global direction.

The global loss function at the t -th training round is then formulated by aggregating the regularized local losses over the selected client devices:

$$\mathcal{L}_g^t = \sum_{i \in \widehat{\mathcal{S}}^t} \widetilde{\mathcal{L}}_i^t. \quad (8)$$

The workflow of GDA is elaborated in **Algorithm 2**.

IV. IMPLEMENTATION

In this section, we first elaborate on the implementation of GAPSL and then present the experiment setup.

A. Implementing GAPSL

We implement the GAPSL prototype using a micro services architecture to support modular deployment and flexible orchestration of both server-side and client-side components, as shown in Fig. 14. The testbed is constructed using NVIDIA Jetson development kits [40]. Specifically, the server is implemented on an NVIDIA Jetson Orin NX, featuring a 1024-core Ampere GPU with 32 Tensor Cores and an 8-core ARM Cortex-A78AE v8.2 64-bit CPU, providing support for server-side FP and BP, as well as coordination mechanisms. To emulate client devices, we adopt NVIDIA Jetson Nano, each equipped with a 128-core Maxwell GPU and a quad-core ARM Cortex-A57 CPU running at 1.43 GHz. Regarding the software stack, we utilize HTTP/2 for the underlying transport protocol to ensure efficient and reliable data transmission and Protocol Buffers for data serialization. The entire system is implemented using Python 3.7, with deep learning tasks executed via PyTorch 1.9.1.

⁶Theoretically, optimizing Eqn. (7) differentiating a loss function that incorporates the local gradient \mathbf{g}_i^t , which necessitates higher-order differentiation (i.e., double backpropagation). To preserve the lightweight nature of GAPSL, our implementation adopts a pragmatic first-order approximation by treating the gradient vectors \mathbf{g}_i^t and $\mathbf{g}_{\text{lead}}^t$ as detached constants from the computational graph. This ensures that the model is updated via standard first-order backpropagation, circumventing the prohibitive overhead of computing second-order derivatives.



Fig. 14: GAPSL prototype and testbed.

1) *Dataset*: To evaluate the learning performance of GAPSL, we adopt two widely used image classification datasets: CIFAR-10 and CIFAR-100 [33]. CIFAR-10 consists of 10 distinct object classes with 50,000 training and 10,000 test images, while CIFAR-100 comprises 100 fine-grained categories, with each category containing 500 training and 100 test samples. In our experiment, we consider both IID and non-IID data settings: i) In the IID setting, the global dataset is randomly shuffled and evenly distributed among all participating client devices, ensuring uniform class distribution and balanced sample sizes; ii) In the non-IID setting, we adopt the Dirichlet data partitioning [34], [35], [36] to set varying degrees of class imbalance controlled by parameter α , where a larger α indicates a more balanced class across edge devices.

2) *Models*: To implement and evaluate GAPSL, we adopt two representative neural network architectures: VGG-16 [32] and Vision Transformer-Base (ViT-Base) [41]. VGG-16 is a standard convolutional neural network composed of 13 convolutional layers followed by 3 fully connected layers. In contrast, ViT-Base is a transformer-based neural network that divides input images into fixed-size patches, embeds them as token sequences, and processes them using stacked transformer blocks with multi-head self-attention. For model partitioning, we split both models into client-side and server-side models for deployments. For VGG-16, the first four convolutional layers are designated as the client-side model, and the remaining layers are deployed as the server-side model. For ViT-Base, the first three transformer blocks constitute the client-side model, with the subsequent blocks processed by the server as the server-side model.

3) *Benchmarks*: To comprehensively evaluate the performance of GAPSL, we compare GAPSL against the following four alternatives:

- **Vanilla SL** is the original version of SL [42], where client-side training is executed sequentially across client devices. In each training round, a single device collaborates with the server to update the model, and the updated client-side model is then passed to the next device for subsequent training.
- **SFL** is the most widely adopted variant of SL that enables parallel client-side training across client devices, where each device updates its client-side model and uploads it to the parameter server for model aggregation [21].
- **PSL** is a variant of SFL (without client-side model synchronization compared with SFL) [26], [27] that trains a shared server-side model using activations from all client devices, while each device independently updates its own

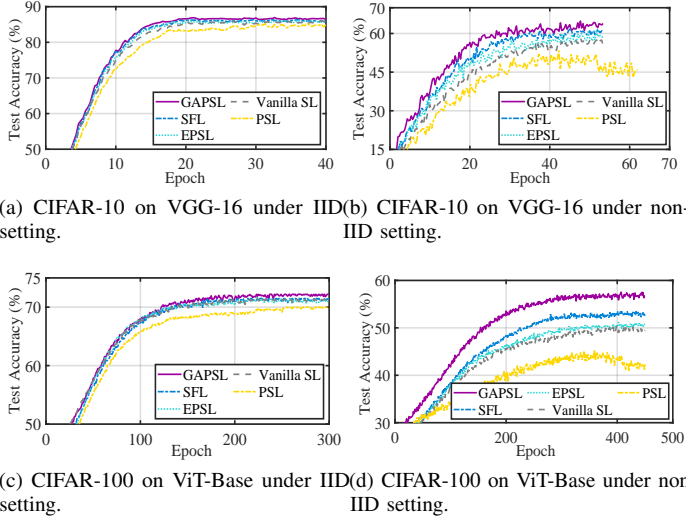


Fig. 15: The training performance for CIFAR-10 and CIFAR-100 under IID and non-IID settings using VGG-16 and ViT-Base.

client-side model based on local datasets.

- **EPSSL** is a variant of PSL [23] that aggregates a portion of the last-layer activation’s gradients on the server to reduce computing and communication overhead.

4) *Hyper-parameters*: In our experiments, we deploy $S = 10$ client devices, and α is set to 0.1 for the non-IID setting by default unless specified otherwise. The regularization coefficient λ is set to 5×10^{-4} for VGG-16 and 3×10^{-5} for ViT-Base. The gradient selection ratio is bounded between $K_{\min} = 20\%$ and $K_{\max} = 80\%$. For model-specific configurations, we use a batch size of 128 for VGG-16 and 64 for ViT-Base. The regularization coefficient λ is set to 5×10^{-4} for VGG-16 and 3×10^{-5} for ViT-Base. For VGG-16, optimization is performed using stochastic gradient descent SGD with a momentum of 0.9. The learning rates are set to 0.005 for client-side training and 0.01 for the server. For ViT-Base, we adopt the AdamW optimizer, with learning rates of 0.0001 for clients and 0.0003 for the server.

V. PERFORMANCE EVALUATION

In this section, we evaluate the performance of GAPSLS from three aspects: i) comparisons with four benchmarks to demonstrate the superiority of GAPSLS; ii) investigating the impact of SL-related hyperparameters on the model performance; iii) ablation studies to show the necessity of each meticulously designed component in GAPSLS, including LGI and GDA.

A. Superiority of GAPSLS

In this section, we conduct a comprehensive comparison of GAPSLS against four benchmarks in terms of test accuracy and convergence speed.

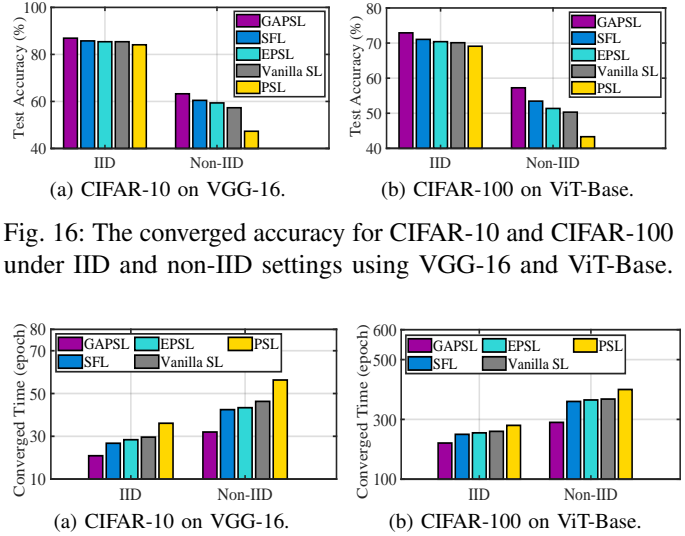


Fig. 16: The converged accuracy for CIFAR-10 and CIFAR-100 under IID and non-IID settings using VGG-16 and ViT-Base.

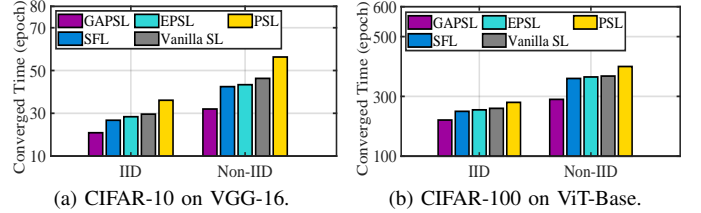


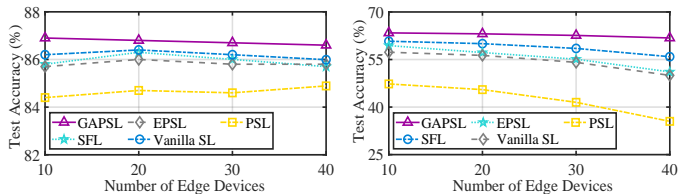
Fig. 17: The converged time for CIFAR-10 and CIFAR-100 under IID and non-IID settings using VGG-16 and ViT-Base.

1) *Training Performance of GAPSLS*: Fig. 15 demonstrates the superior performance of GAPSLS over four benchmarks on CIFAR-10 and CIFAR-100 datasets under IID and non-IID settings. GAPSLS consistently achieves higher accuracy and faster convergence speed across both IID and non-IID settings. This performance gain is primarily attributed to the synergistic design of LGI and GDA, which effectively identifies the global optimization direction and rectifies local gradient updates via gradient direction alignment. Specifically, the performance gap between GAPSLS and PSL reveals the advantage of our tailored GDA scheme, which employs direction-aware regularization to mitigate local bias and expedite convergence. While data heterogeneity induces severe gradient conflicts, GAPSLS demonstrates remarkable resilience, effectively resolving gradient inconsistency to maintain robust convergence toward the global optimum. In contrast, vanilla SL and PSL exhibit significant performance degradation, particularly under non-IID settings, due to their lack of statistical gradient calibration. Although SFL and EPSSL offer moderate gains through model aggregation or partial synchronization, they still fall short of the efficacy achieved by GAPSLS. By comparing Fig. 15a with Fig. 15b, and Fig. 15c with Fig. 15d, we show that GAPSLS and the other four benchmarks experience slower convergence under the non-IID setting than the IID setting.

2) *Converged Accuracy of GAPSLS*: Fig. 16 illustrates the converged accuracy of GAPSLS against four other benchmarks on CIFAR-10 and CIFAR-100 datasets. In the non-IID setting,

TABLE I: Test accuracy (%) and convergence time (epochs) on CIFAR-10 and CIFAR-100.

Dataset	Model	Metric (Setting)	GAPSLS	SFL	EPSSL	Vanilla SL	PSL
CIFAR-10	VGG-16	Accuracy (IID)	86.9	86.2	85.8	85.7	84.3
		Accuracy (Non-IID)	63.3	60.7	59.4	57.3	47.3
		Time (IID)	21	27	28	29	36
		Time (Non-IID)	32	42	43	46	56
CIFAR-100	ViT-Base	Accuracy (IID)	72.1	71.5	70.8	70.7	69.8
		Accuracy (Non-IID)	57.0	53.4	51.4	50.3	43.2
		Time (IID)	220	254	254	261	283
		Time (Non-IID)	290	361	366	369	401



(a) CIFAR-10 on VGG-16 under IID (b) CIFAR-10 on VGG-16 under non-IID setting.

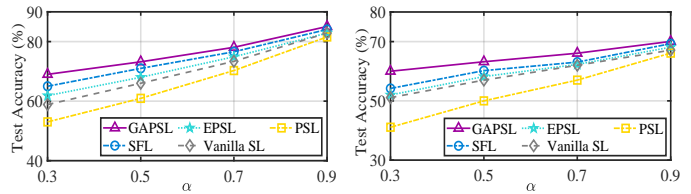
Fig. 18: The test accuracy versus number of edge devices on CIFAR-10 under IID and non-IID settings using VGG-16.

TABLE II: Test accuracy (%) versus number of devices on CIFAR-10 using VGG-16.

Setting	Devices Scale	GAPSL	SFL	EPSSL	Vanilla SL	PSL
IID	10	86.9	86.2	85.8	85.7	84.3
	20	86.8	86.4	86.3	86.1	84.7
	30	86.7	86.2	86.0	85.8	84.6
	30	86.7	86.2	86.0	85.8	84.6
	40	86.5	85.9	85.7	85.7	84.9
Non-IID	10	63.3	60.7	59.4	57.3	47.3
	20	63.1	60.1	57.2	56.3	45.5
	30	62.6	58.5	55.1	54.2	41.4
	30	62.6	58.5	55.1	54.2	41.4
	40	61.7	55.9	55.3	50.1	35.6

both PSL and vanilla SL suffer from substantial accuracy degradation, with an accuracy drop of approximately 37.0% (resp. 26.6%) and 28.4% (resp. 20.4%) on CIFAR-10 (resp. CIFAR-100) relative to their IID counterparts. This degradation in PSL is attributed to the lack of gradient coordination, which induces directional inconsistency and suboptimal updates. Vanilla SL is plagued by catastrophic forgetting inherent to its sequential training paradigm, where round-robin updates over heterogeneous data lead to overfitting on recent samples and the erasure of prior knowledge. While SFL and EPSSL mitigate these issues via partial aggregation or synchronization, they still incur noticeable accuracy losses due to their limited capability in resolving severe gradient conflicts. In contrast, GAPSL demonstrates superior robustness, outperforming SFL, EPSSL, vanilla SL, and PSL by margins of 2.6% (resp. 3.6%), 3.9% (resp. 5.6%), 6.0% (resp. 6.7%), and 16.0% (resp. 13.8%) on CIFAR-10 (resp. CIFAR-100) under the non-IID setting. This significant improvement validates the effectiveness of our design, where LGI extracts directionally consistent trends, and GDA enforces rigorous alignment across client devices.

3) *Converged Time of GAPSL*: Fig. 17 compares the converged time of GAPSL against four other benchmarks on CIFAR-10 and CIFAR-100 datasets. In the IID setting, SFL, EPSSL, vanilla SL, and PSL take approximately 1.3 \times (resp. 1.2 \times), 1.3 \times (resp. 1.2 \times), 1.4 \times (resp. 1.2 \times), and 1.7 \times (resp. 1.3 \times) more epochs to converge than GAPSL on CIFAR-10 (resp. CIFAR-100). This notable performance gain is attributed to the synergistic design of LGI and GDA. Specifically, LGI effectively filters out divergent updates to extract a lead gradient that reflects the global optimization direction, while GDA rigorously aligns local gradients with this reference. This selective and adaptive design effectively suppresses gradient noise and expedites model convergence. In contrast, vanilla SL exhibits the slowest convergence due to its inherently sequential training paradigm. SFL, EPSSL, and PSL suffer from



(a) CIFAR-10 on VGG-16.

(b) CIFAR-100 on ViT-Base.

Fig. 19: The test accuracy versus degrees of data heterogeneity on CIFAR-10 and CIFAR-100 using VGG-16 and ViT-Base.

TABLE III: Test accuracy (%) versus data heterogeneity (Dirichlet α) on CIFAR-10 and CIFAR-100.

Dataset	Model	α	GAPSL	SFL	EPSSL	Vanilla SL	PSL
CIFAR-10	VGG-16	0.9	85.0	84.1	82.8	82.7	81.3
		0.7	78.1	76.6	74.9	73.4	70.3
		0.5	73.2	71.2	68.0	66.2	60.9
		0.5	73.2	71.2	68.0	66.2	60.9
		0.3	69.3	65.1	61.8	58.9	53.5
CIFAR-100	ViT-Base	0.9	70.1	69.3	68.2	67.3	66.1
		0.7	66.2	63.1	62.3	62.0	57.4
		0.5	63.4	60.2	58.2	57.1	50.0
		0.5	63.4	60.2	58.2	57.1	50.0
		0.3	60.6	54.3	52.1	51.4	41.2

prolonged training latencies caused by inconsistent gradient directions across devices. In the non-IID setting, where data heterogeneity exacerbates gradient divergence and optimization drift, all methods experience increased convergence times. Nevertheless, GAPSL still maintains the shortest converged time, demonstrating superior robustness and adaptability to statistical heterogeneity. Detailed numerical results are summarized in Table I.

B. Micro-benchmarking

In this section, we investigate the impact of hyperparameters on the model performance.

1) *Impact of Number of Edge Devices*: Fig. 18 shows the converged accuracy of GAPSL and other benchmarks versus the number of edge devices on CIFAR-10 and CIFAR-100 datasets under IID and non-IID settings. GAPSL consistently achieves the highest test accuracy across varying numbers of edge devices, demonstrating strong scalability and robustness to the device scale. In the IID setting, all benchmarks exhibit marginal accuracy changes as the number of devices increases, benefiting from the uniform data distribution across edge devices. Nevertheless, GAPSL illustrates the highest accuracy, attributed to its direction-aware gradient alignment mechanism that preserves cross-device gradient consistency. In contrast, all benchmarks suffer from significant accuracy drops with increasing device scale in the non-IID setting, which is caused by the exacerbated gradient inconsistency on highly heterogeneous data. However, GAPSL exhibits remarkable resilience, showing only a negligible accuracy decline even as the system scales to 40 client devices. This robustness is underpinned by the synergistic design of LGI and GDA that effectively mitigates the gradient inconsistency caused by data heterogeneity. These observations validate the superior scalability of GAPSL for large-scale edge computing systems. Detailed numerical results are summarized in Table II.

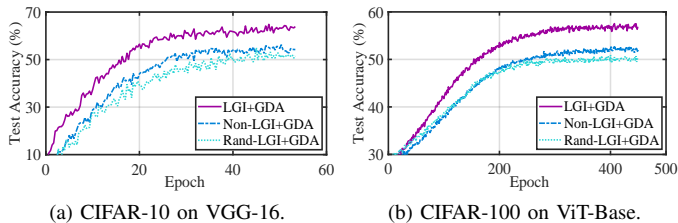


Fig. 20: The ablation evaluation for LGI on CIFAR-10 and CIFAR-100 under non-IID setting using VGG-16 and ViT-Base.

2) *Impact of Data Heterogeneity*: Fig. 19 illustrates the converged accuracy of GAPSL and other benchmarks versus the degree of data heterogeneity on CIFAR-10 and CIFAR-100 datasets. It can be seen that all benchmarks experience a noticeable decline in model accuracy as the degree of data heterogeneity increases (indicated by a decrease in α). Specifically, PSL exhibits the most severe performance degradation, with accuracy dropping by up to 27.8% (resp. 24.9%) on CIFAR-10 (resp. CIFAR-100) as α decreases from 0.9 to 0.3. This sharp decline stems from its lack of client-side aggregation, which exacerbates gradient divergence in the non-IID setting. While SFL and EPSL exhibit moderate accuracy loss, they benefit partially from model aggregation or partial gradient synchronization. In contrast, GAPSL consistently maintains superior accuracy across varying data heterogeneity. Even in a highly non-IID setting, GAPSL incurs only a minimal accuracy reduction. This superior resilience showcases the effectiveness of GAPSL’s design in mitigating the adverse effects of data heterogeneity, underscoring its scalability and stability on heterogeneous data. Detailed numerical results are summarized in Table III.

C. Ablation Study

This section evaluates the impact of each module of GAPSL on the model performance.

1) *Leader Gradient Identification*: Fig. 20 shows the impact of LGI on training performance under the non-IID setting. We compare the training performance of LGI with two ablated variants: Non-LGI, which aggregates gradients from all devices to construct a leader gradient without gradient filtering, and Rand-LGI, which constructs the leader gradient via random gradient subset selection. The results demonstrate that LGI consistently yields superior test accuracy compared to both variants. This advantage stems from LGI’s directional consistency-aware gradient selection, which dynamically identifies and aggregates only directionally consistent gradients. In contrast, Non-LGI suffers from noticeable performance degradation due to the inclusion of conflicting gradients that destabilize the update direction. Rand-LGI exhibits even worse performance, indicating that random selection fails to capture the underlying convergence trend, leading to unstable updates and poor generalization. Notably, the performance gap between LGI and its ablated variants is more pronounced in the ViT-Base model than in VGG-16. This suggests that deeper and more

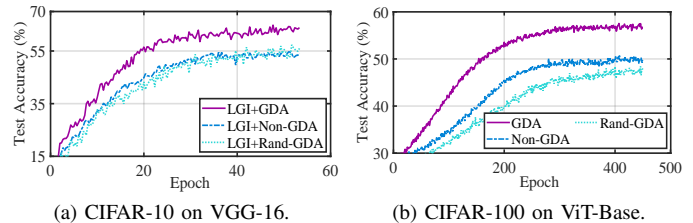


Fig. 21: The ablation evaluation for GDA on CIFAR-10 and CIFAR-100 using VGG-16 and ViT-Base under non-IID setting.

complicated transformer-based architectures are more sensitive to gradient inconsistency and thus benefit more significantly from the robust gradient filtering provided by LGI.

2) *Gradient Direction Alignment*: Fig. 21 shows the impact of GDA on training performance under the non-IID setting. We compare GDA with two ablated variants: Non-GDA, which removes the gradient alignment mechanism and relies solely on the leader gradient for model update, and Rand-GDA, which employs gradient alignment randomly to a subset of local gradients, regardless of their angular deviation from the leader gradient. The results demonstrate that GDA exhibits the highest test accuracy, which is attributed to GDA’s adaptive regularization, which imposes a geometric constraint on each device’s loss function to align its gradients with the global convergence direction. In contrast, Non-GDA exhibits the lowest accuracy due to the absence of alignment, which causes local gradients to deviate significantly from the global objective. Rand-GDA performs marginally better, but its random alignment fails to ensure consistent updates, resulting in unstable optimization and reduced generalization. These observations confirm the essential role of GDA in improving convergence stability and enhancing model performance.

VI. RELATED WORK

1) *Split Learning*. SL has emerged as a promising privacy-enhancing distributed learning paradigm to address the limitations of FL. Vepakomma *et al.* [42] first proposed the original SL, known as vanilla SL, where clients collaborate with the server in a round-robin manner for co-training; however, this client-side sequential training manner suffers from excessive training latency. To enable client-side parallel training, Thepa *et al.* [21] developed the most prevalent SL variant, coined SFL, that integrates model partitioning of SL with parallel training of FL to parallelize the client-side model training, enabling multiple devices to collaboratively train a shared model. Building upon this, Kim *et al.* and Joshi *et al.* [26], [27] devised the PSL framework that eliminates client-side model aggregation to streamline the training procedure of SFL, accelerating model convergence while compromising the training performance. Subsequent research endeavors have been dedicated to developing more communication- and computation-efficient SL. Lin *et al.* [23] designed an efficient PSL framework that employs last-layer gradient aggregation to shrink the dimensionality of activations’ gradients for reducing the training latency. Pal *et al.* [43] devised a more scalable PSL framework

that averages the local gradients at the cut layer to overcome server-side large batch and the backward client decoupling problems. Lin *et al.* [44], [45] derived a theoretical convergence analysis for SFL and proposed an efficient algorithm to adaptively control model splitting and sub-model aggregation interval.

2) *Data Heterogeneity Mitigation*. Research efforts to mitigate data heterogeneity in distributed learning predominantly focus on FL, with two major research directions: model aggregation optimization, which aims to reduce update bias in model aggregation, and data-adaptive personalization, which seeks to tailor models to individual devices' data distributions instead of forcing a single global model to fit all. For *model aggregation optimization*, Shi *et al.* [46] proposed FedAWA that adaptively adjusts aggregation weights based on the direction of client model updates, eliminating the need for additional data and thereby enhancing both the stability and generalization of the global model. Karimireddy *et al.* [47] developed SCAFFOLD that controls variance reduction in model aggregation to reduce client-drift, thus achieving model convergence with fewer communication rounds. Deng *et al.* [31] proposed a cell-wise shared model layer selection to adaptively construct the shared architecture across devices, followed by a cell-based aggregation strategy tailored to device-specific architectures. For *data-adaptive personalization*, Wu *et al.* [48] devised FedCache that reserves a server-side knowledge cache for fetching personalized knowledge from the samples with similar hashes and then employs ensemble distillation to personalize local models for local bias mitigation. Hu *et al.* [34] designed a clustered data sharing FL framework that selectively shares partial data from cluster heads to trusted associates via sidelink multicasting to mitigate data heterogeneity. Wang *et al.* [49] proposed pFedHR, which generates diverse personalized models and applies model reassembly to alleviate the adverse effects of data heterogeneity.

While the above frameworks have demonstrated effectiveness under data heterogeneity, they typically rely on full model aggregation and frequent global synchronization, which is inherently incompatible with the PSL that eliminates client-side aggregation via model partitioning. As a result, the design of PSL tailored to data heterogeneity is still void.

VII. CONCLUSION

Taking an important step towards the SL paradigm, we have proposed a cutting-edge gradient-aligned PSL framework, named GAPSL, enabling efficient model training without client-side model aggregation. GAPSL comprises two key components: leader gradient identification and gradient direction alignment. First, the leader gradient identification mechanism selects and aggregates a subset of directionally consistent client gradients to construct a leader gradient reflecting the global convergence direction. Second, the gradient direction alignment scheme aligns each device's gradient with the leader gradient via a direction-aware regularization term to improve model convergence. The experimental results demonstrate that GAPSL achieves superior performance compared to state-of-the-art benchmarks.

REFERENCES

- [1] Y. Liu, C. Wang, and X. Yuan, "FedMobile: Enabling Knowledge Contribution-aware Multi-modal Federated Learning with Incomplete Modalities," in *Proc. WWW*, 2025, pp. 2775–2786.
- [2] Z. Fang, Z. Lin, S. Hu, Y. Tao, Y. Deng, X. Chen, and Y. Fang, "Dynamic Uncertainty-Aware Multimodal Fusion for Outdoor Health Monitoring," *arXiv preprint arXiv:2508.09085*, 2025.
- [3] F. Sarhaddi, N. T. Nguyen, A. Zuniga, P. Hui, S. Tarkoma, H. Flores, and P. Nurmi, "LLMs and IoT: A Comprehensive Survey on Large Language Models and the Internet of Things," *Authorea Preprints*, 2025.
- [4] Z. Fang, Z. Lin, S. Hu, Y. Ma, Y. Tao, Y. Deng, X. Chen, and Y. Fang, "Hfedmoe: Resource-Aware Heterogeneous Federated Learning with Mixture-of-Experts," *arXiv preprint arXiv:2601.00583*, 2026.
- [5] Y. Li, H. Wang, W. Xu, T. Xiao, H. Liu, M. Tu, Y. Wang, X. Yang, R. Zhang, S. Yu *et al.*, "Unleashing the Power of Continual Learning on Non-centralized Devices: A Survey," *IEEE Commun. Surv. Tutor.*, 2025.
- [6] T. Subramanya and R. Riggio, "Centralized and Federated Learning for Predictive VNF Autoscaling in Multi-domain 5G Networks and Beyond," *IEEE Trans. Netw. Serv. Manag.*, vol. 18, no. 1, pp. 63–78, 2021.
- [7] A.-R. Ottun, P. C. Mane, Z. Yin, S. Paul, M. Liyanage, J. Pridmore, A. Y. Ding, R. Sharma, P. Nurmi, and H. Flores, "Social-aware Federated Learning: Challenges and Opportunities in Collaborative Data Training," *IEEE Internet Comput.*, vol. 27, no. 2, pp. 36–44, 2022.
- [8] Z. Fang, Z. Lin, Z. Chen, X. Chen, Y. Gao, and Y. Fang, "Automated Federated Pipeline for Parameter-efficient Fine-tuning of Large Language Models," *IEEE Trans. Mobile Comput.*, Apr. 2025.
- [9] "Amount of Data Created, Consumed, and Stored 2010-2023, with Forecasts to 2028," Statista. May. 2024. [Online]. Available: <https://www.statista.com/statistics/871513/worldwide-data-created/>
- [10] X. Liu, Z. Yan, Y. Zhou, D. Wu, X. Chen, and J. H. Wang, "Optimizing Parameter Mixing Under Constrained Communications in Parallel Federated Learning," *IEEE/ACM Trans. Networking*, vol. 31, no. 6, pp. 2640–2652, Dec. 2023.
- [11] Y. Deng, X. Chen, G. Zhu, Y. Fang, Z. Chen, and X. Deng, "Actions at the Edge: Jointly Optimizing the Resources in Multi-access Edge Computing," *IEEE Wireless Commun.*, vol. 29, no. 2, pp. 192–198, Apr. 2022.
- [12] B. McMahan, E. Moore, D. Ramage, S. Hampson, and B. A. Arcas, "Communication-efficient Learning of Deep Networks From Decentralized Data," in *Proc. AISTATS*, Apr. 2017.
- [13] J. Konečný, H. B. McMahan, F. X. Yu, P. Richtárik, A. T. Suresh, and D. Bacon, "Federated Learning: Strategies for Improving Communication Efficiency," *arXiv preprint arXiv:1610.05492*, Oct. 2016.
- [14] M. Hu, J. Zhang, X. Wang, S. Liu, and Z. Lin, "Accelerating Federated Learning with Model Segmentation for Edge Networks," *IEEE Trans. Green Commun. Netw.*, Jul. 2024.
- [15] W. Chen, C. Yang, J. Ren, Z. Li, and Z. Wang, "Optimizing Personalized Federated Learning through Adaptive Layer-Wise Learning," in *Proc. IJCAI*, 2024.
- [16] J. Zheng, J. Xu, H. Du, D. Niyato, J. Kang, J. Nie, and Z. Wang, "Trust Management of Tiny Federated Learning in Internet of Unmanned Aerial Vehicles," *IEEE Internet Things J.*, vol. 11, no. 12, pp. 21 046–21 060, 2024.
- [17] Z. Lin, Y. Zhang, Z. Chen, Z. Fang, X. Chen, P. Vepakomma, W. Ni, J. Luo, and Y. Gao, "HSplitLoRA: A Heterogeneous Split Parameter-Efficient Fine-Tuning Framework for Large Language Models," *arXiv preprint arXiv:2505.02795*, 2025.
- [18] W. Wu, M. Li, K. Qu, C. Zhou, X. Shen, W. Zhuang, X. Li, and W. Shi, "Split learning over Wireless Networks: Parallel Design and Resource Management," *IEEE J. Sel. Areas Commun.*, vol. 41, no. 4, pp. 1051–1066, Feb. 2023.
- [19] G. Team, R. Anil, S. Borgeaud, J.-B. Alayrac, J. Yu, R. Soricut, J. Schalkwyk, A. M. Dai, A. Hauth, K. Millican *et al.*, "Gemini: A Family of Highly Capable Multimodal Models," *arXiv preprint arXiv:2312.11805*, Dec. 2023.
- [20] Z. Lin, Z. Chen, X. Chen, W. Ni, and Y. Gao, "HASFL: Heterogeneity-aware Split Federated Learning over Edge Computing Systems," *IEEE Trans. Mobile Comput.*, 2026.
- [21] C. Thapa, P. C. M. Arachchige, S. Camtepe, and L. Sun, "Splitfed: When Federated Learning Meets Split Learning," in *Proc. AAAI*, Feb. 2022.
- [22] D. Pasquini, G. Ateniese, and M. Bernaschi, "Unleashing the Tiger: Inference Attacks on Split Learning," in *Proc. CCS*, Nov. 2021.
- [23] Z. Lin, G. Zhu, Y. Deng, X. Chen, Y. Gao, K. Huang, and Y. Fang, "Efficient Parallel Split Learning over Resource-constrained Wireless Edge Networks," *IEEE Trans. Mobile Comput.*, 2024.

- [24] Z. Fang, M. Yang, Z. Lin, Z. Lin, Z. Fang, Z. Zhang, T. Duan, D. Huang, and S. Zhu, "NSC-SL: A Bandwidth-Aware Neural Subspace Compression for Communication-Efficient Split Learning," in *Proc. ICASSP*, 2026.
- [25] Z. Lin, Y. Zhang, Z. Chen, Z. Fang, Y. Yang, G. Zhang, H. Yang, C. Wu, X. Chen, and Y. Gao, "ESL-LEO: An Efficient Split Learning Framework over LEO Satellite Networks," in *Proc. WASA*, 2025.
- [26] M. Kim, A. DeRieux, and W. Saad, "A Bargaining Game for Personalized, Energy Efficient Split Learning over Wireless Networks," *arXiv preprint arXiv:2212.06107*, Dec. 2022.
- [27] P. Joshi, C. Thapa, S. Camtepe, M. Hasanuzzamana, T. Scully, and H. Afi, "Splitfed Learning Without Client-side Synchronization: Analyzing Client-side Split Network Portion Size to Overall Performance," *arXiv preprint arXiv:2109.09246*, Sep. 2021.
- [28] Z. Lin, G. Qu, X. Chen, and K. Huang, "Split Learning in 6G Edge Networks," *IEEE Wireless Commun.*, 2024.
- [29] T. Yu, J. Wang, H. Wang, M. Lin, H. Liu, N. S. Yee, and F. Ma, "Towards Collaborative Fairness in Federated Learning Under Imbalanced Covariate Shift," in *Proc. SIGKDD*, 2025, pp. 3645–3656.
- [30] Z. Li, Z. Lin, J. Shao, Y. Mao, and J. Zhang, "FedCiR: Client-invariant Representation Learning for Federated Non-IID Features," *IEEE Trans. Mobile Comput.*, vol. 23, no. 11, pp. 10 509–10 522, 2024.
- [31] D. Deng, X. Wu, T. Zhang, X. Tang, H. Du, J. Kang, J. Liu, and D. Niyato, "FedASA: A Personalized Federated Learning with Adaptive Model Aggregation for Heterogeneous Mobile Edge Computing," *IEEE Trans. Mobile Comput.*, 2024.
- [32] K. Simonyan and A. Zisserman, "Very Deep Convolutional Networks for Large-scale Image Recognition," in *Proc. ICLR*, 2015.
- [33] A. Krizhevsky, G. Hinton *et al.*, "Learning Multiple Layers of Features From Tiny Images," *Tech. Rep.*, Apr. 2009.
- [34] G. Hu, Y. Teng, N. Wang, and Z. Han, "Faster Convergence on Heterogeneous Federated Edge Learning: An Adaptive Clustered Data Sharing Approach," *IEEE Trans. Mobile Comput.*, 2025.
- [35] Z. Lin, Y. Zhang, Z. Chen, Z. Fang, C. Wu, X. Chen, Y. Gao, and J. Luo, "LEO-Split: A Semi-supervised Split Learning Framework over LEO Satellite Networks," *IEEE Trans. Mobile Comput.*, 2025.
- [36] R. Zhang, Y. Chen, C. Wu, F. Wang, and B. Li, "Multi-level Personalized Federated Learning on Heterogeneous and Long-tailed Data," *IEEE Trans. Mobile Comput.*, vol. 23, no. 12, pp. 12 396–12 409, 2024.
- [37] H. Wang, W. Xu, Y. Fan, R. Li, and P. Zhou, "AOCC-FL: Federated Learning with Aligned Overlapping via Calibrated Compensation," in *Proc. IEEE INFOCOM*, 2023.
- [38] T. Song, Y. Tong, and S. Wei, "Profit Allocation for Federated Learning," in *Proc. Big Data*, 2019.
- [39] Z. Lian, J. Cao, Z. Zhu, X. Zhou, and W. Liu, "GOFL: An accurate and efficient federated learning framework based on gradient optimization in Heterogeneous IoT systems," *IEEE Internet Things J.*, vol. 11, no. 7, pp. 12 459–12 474, 2023.
- [40] (2024) "NVIDIA Jetson Embedded Systems Developer Kits and Modules". Available: <https://www.nvidia.cn/autonomous-machines/embedded-systems/?section=jetsonTX2>.
- [41] A. Dosovitskiy, L. Beyer, A. Kolesnikov, D. Weissenborn, X. Zhai, T. Unterthiner, M. Dehghani, M. Minderer, G. Heigold, S. Gelly *et al.*, "An Image is Worth 16x16 Words: Transformers for Image Recognition at Scale," in *Proc. ICLR*, 2021.
- [42] P. Vepakomma, O. Gupta, T. Swedish, and R. Raskar, "Split Learning for Health: Distributed Deep Learning without Sharing Raw Patient Data," *arXiv preprint arXiv:1812.00564*, Dec. 2018.
- [43] S. Pal, M. Uniyal, J. Park, P. Vepakomma, R. Raskar, M. Bennis, M. Jeon, and J. Choi, "Server-side Local Gradient Averaging and Learning Rate Acceleration for Scalable Split Learning," *arXiv preprint arXiv:2112.05929*, Dec. 2021.
- [44] Z. Lin, G. Qu, W. Wei, X. Chen, and K. K. Leung, "Adaptsfl: Adaptive Split Federated Learning in Resource-constrained Edge Networks," *IEEE Trans. Networking*, Jul. 2025.
- [45] Z. Lin, W. Wei, Z. Chen, C.-T. Lam, X. Chen, Y. Gao, and J. Luo, "Hierarchical Split Federated Learning: Convergence Analysis and System Optimization," *IEEE Trans. Mobile Comput.*, Dec. 2024.
- [46] C. Shi, H. Zhao, B. Zhang, M. Zhou, D. Guo, and Y. Chang, "FedAWA: Adaptive Optimization of Aggregation Weights in Federated Learning Using Client Vectors," in *Proc. CVPR*, 2025.
- [47] S. P. Karimireddy, S. Kale, M. Mohri, S. Reddi, S. Stich, and A. T. Suresh, "Scaffold: Stochastic Controlled Averaging for Federated Learning," in *Proc. ICML*, Apr. 2020.
- [48] Z. Wu, S. Sun, Y. Wang, M. Liu, K. Xu, W. Wang, X. Jiang, B. Gao, and J. Lu, "Fedcache: A Knowledge Cache-driven Federated Learning Architecture for Personalized Edge Intelligence," *IEEE Trans. Mobile Comput.*, vol. 23, no. 10, pp. 9368–9382, 2024.
- [49] J. Wang, X. Yang, S. Cui, L. Che, L. Lyu, D. D. Xu, and F. Ma, "Towards Personalized Federated Learning via Heterogeneous Model Reassembly," *Proc. NIPS*, 2023.